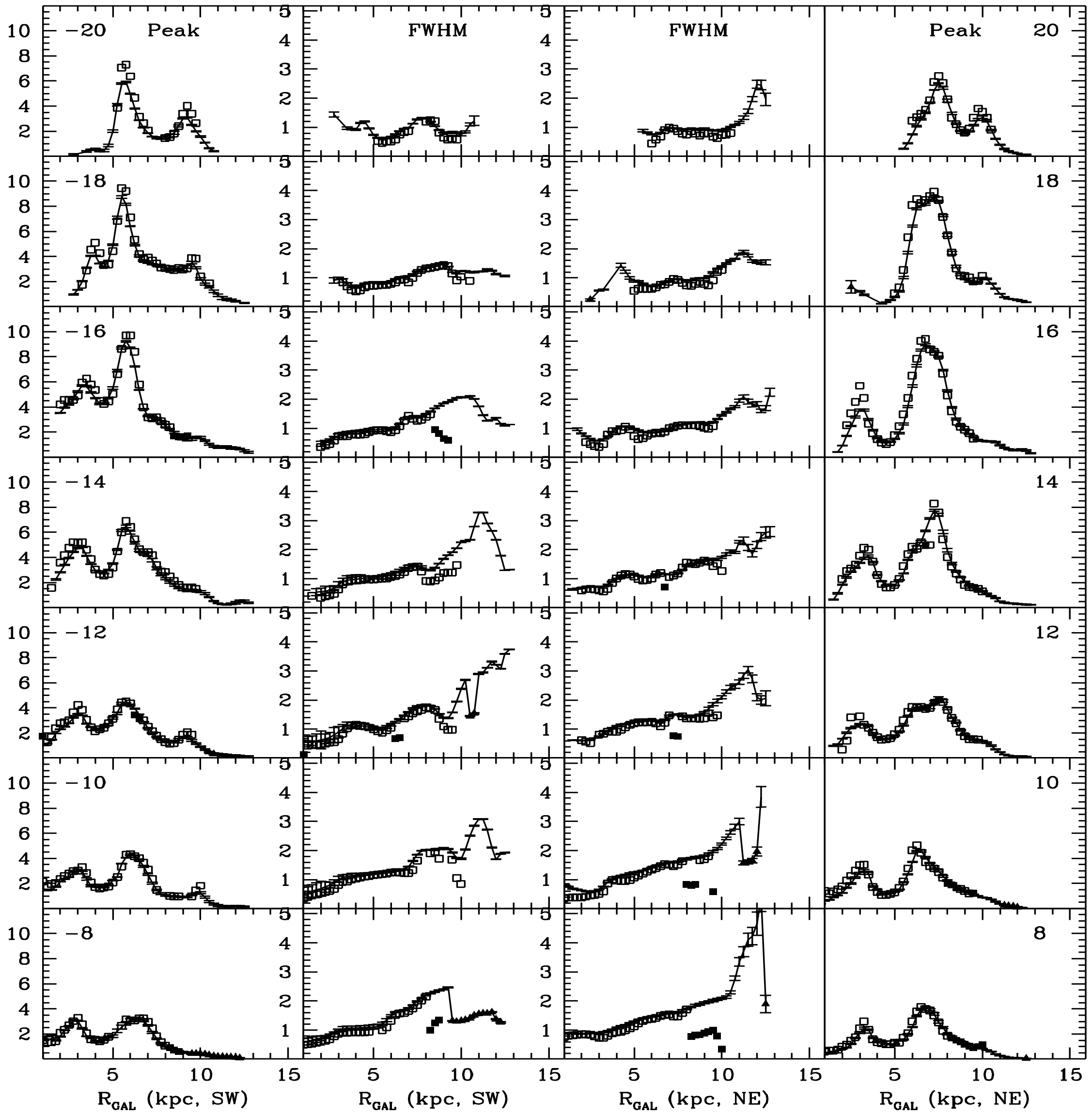

Fig. 26.— In this figure the results of the Gaussian fits to the channel maps are presented. The middle two panels show the measured widths ($FWHM$, beam size corrected, in units of kpc), the outer two panels show the fitted peaks ($M_\odot\,\mathrm{pc}^{-2}$, beam size corrected). The results obtained from the (10.″1 x 28.″3, 177x495 pc) channel maps are represented by the open squares, the fits to the intermediate resolution (38″ , 665 pc) maps by the full line (with error bars). At few positions two component fits could be made, these are indicated by filled symbols (filled triangles for the intermediate resolution data). The two left-hand panels are determined from the south-western side, the two right-hand panels from the north-eastern side.

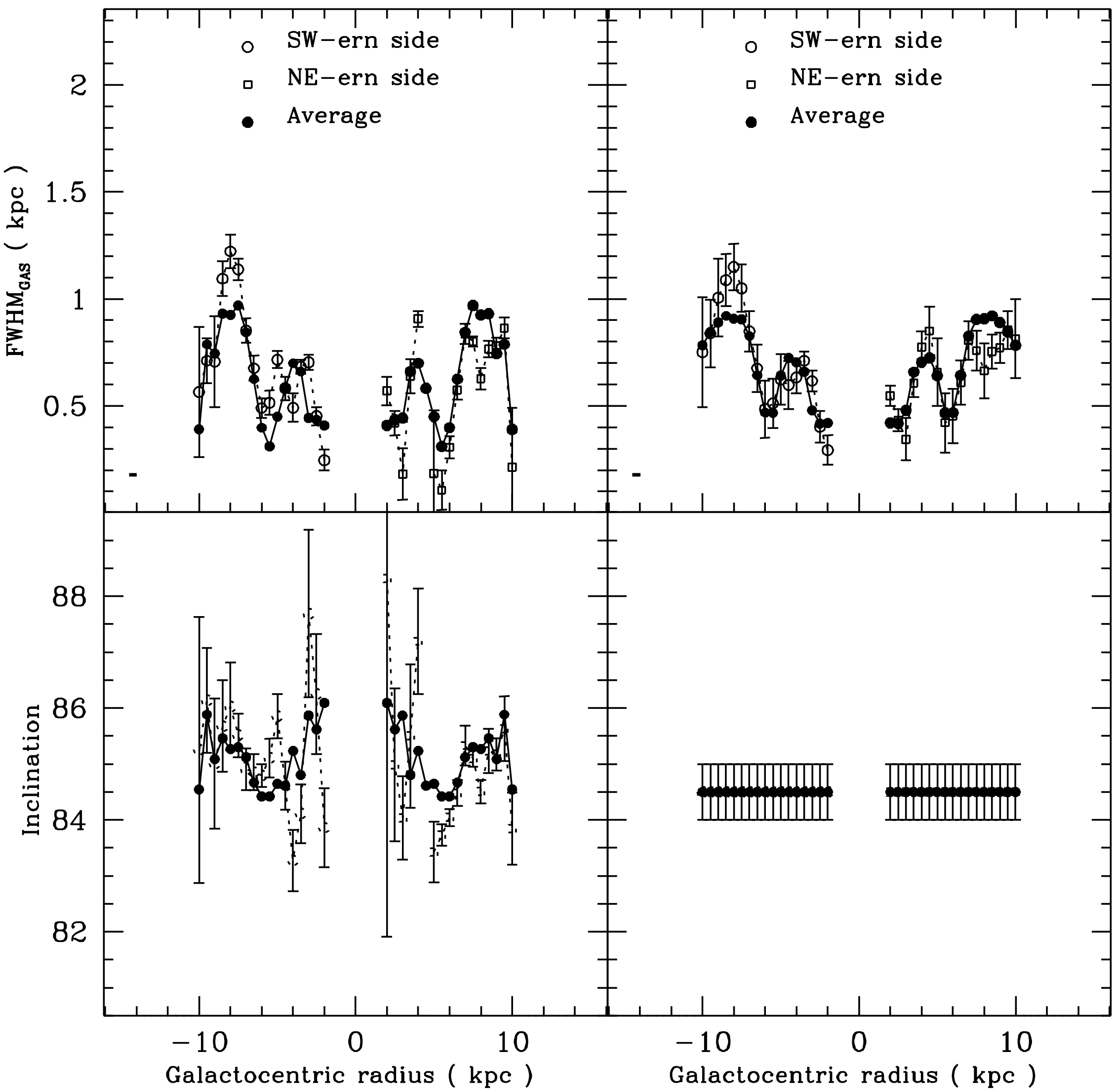

Fig. 27.— Here I present the thickness (upper panel) and inclination (lower panel) derived from the fitted widths (at 10.″1 resolution) presented in Fig. 26 using the procedure described in Sec. 3.5.1.. Both sides (south-western part on the left) of the galaxy are shown. The fat bar in the lower left corner of the top panel represents the size of the beam, horizontally and vertically for the major axis and minor axis, respectively. For the panels on the left hand side I allowed the inclination to vary, the panels on the right hand side are calculated with a fixed inclination of 84.5°. The filled circles represent the average of both sides. The weighting scheme which takes potential errors due to streaming motions into account was used (see Appendix 3.12.).

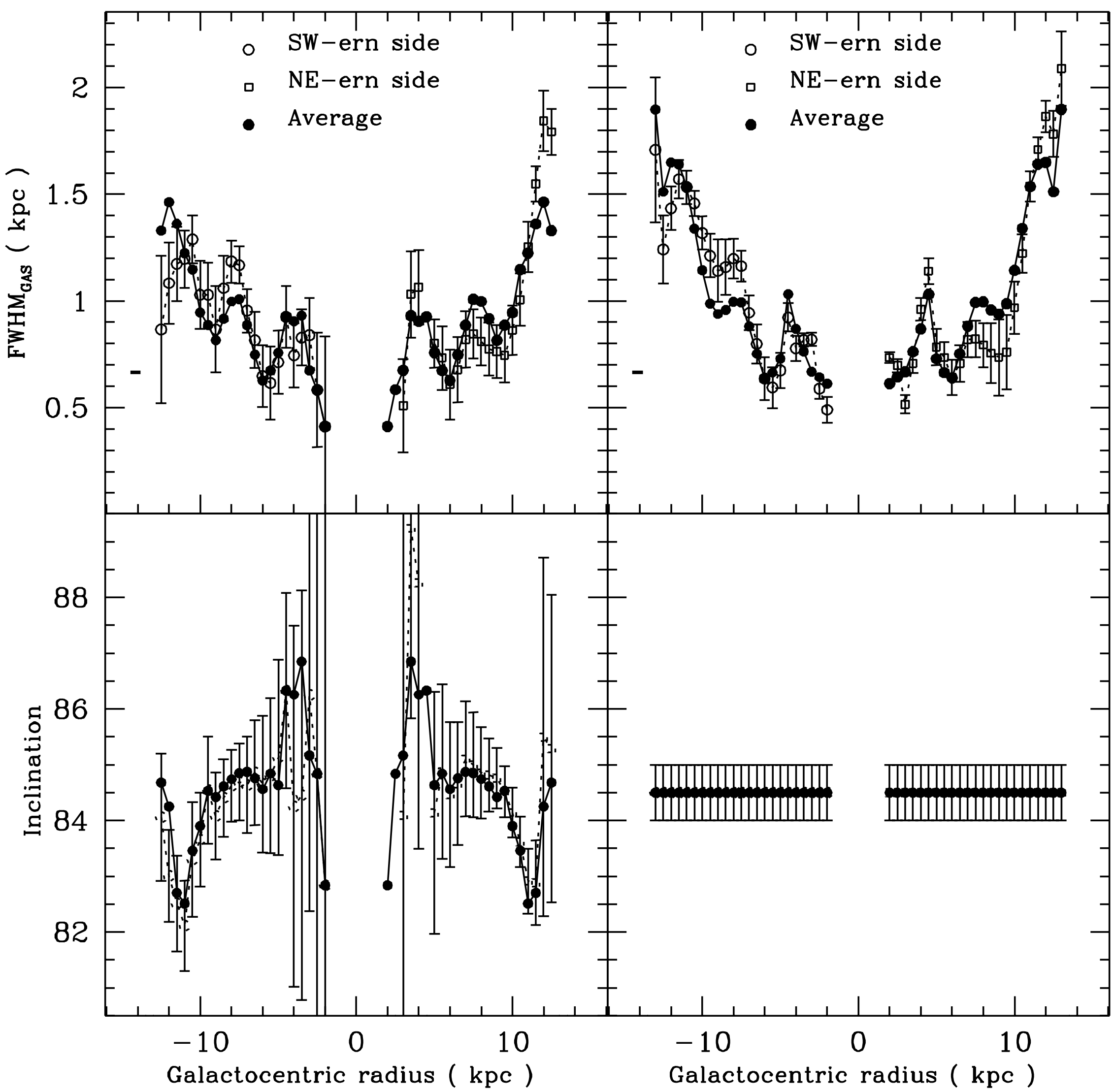

Fig. 27b.— Thickness and inclination as derived from the 38″ x 38″ resolution channel maps.

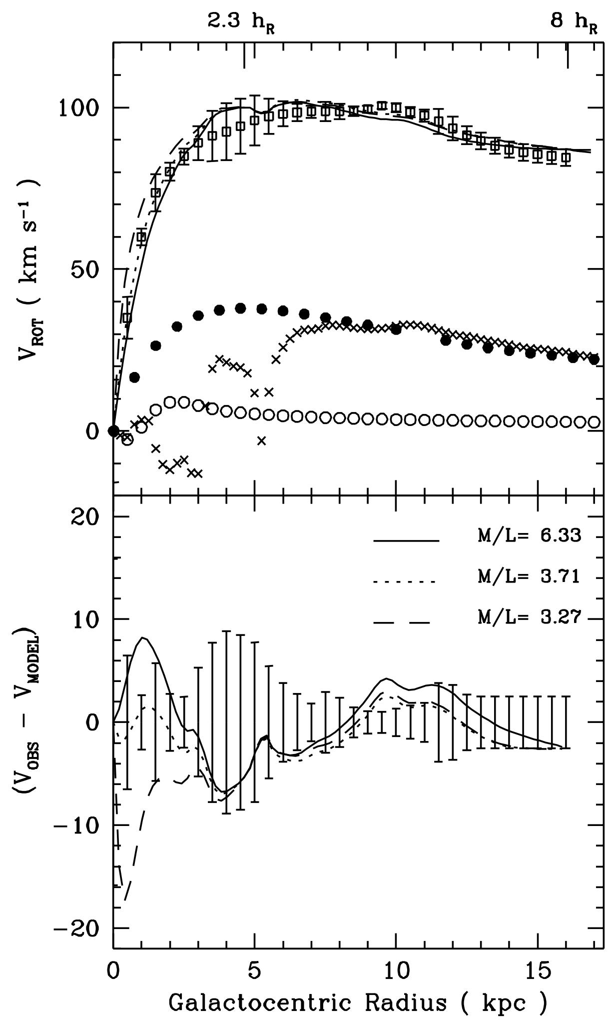

Fig. 28.— The top panel shows disk-halo decompositions of the observed rotation curve (squares with error bars) into components due to the gaseous disks (H I ,crosses; H_2, open circles), a component due to the stellar disk (vertically sech^2 and radially exponential till R_{max}=10 kpc, $M/\mathcal{L}_B$ =1; filled circles) and a DM component. The individual contributing DM components are not shown. The values for the model rotation curve at $2.3h_R$ and $8h_R$ have been adjusted (to 99 and 87 km s^{-1}) such as to minimize the residuals (lower panel). All three disk-halo decompositions ($[M/\mathcal{L}_B = 6.16, R_c = 12 \text{ kpc}, \rho_{h,0} = 1.57 \text{ m}M_\odot/\text{pc}^3]$ full line, $[M/\mathcal{L}_B = 3.49, R_c = 0.63, \rho_{h,0} = 252]$ dotted line, $[M/\mathcal{L}_B = 3.12, R_c = 0.32, \rho_{h,0} = 972]$ dashed line) represent the observations equally well. For the disk-halo decompositions presented here, the f_m, f_8, and β_8 parameters (as defined in Chapter 2) have the values 0.7094, 0.6033, and 0.861 respectively.

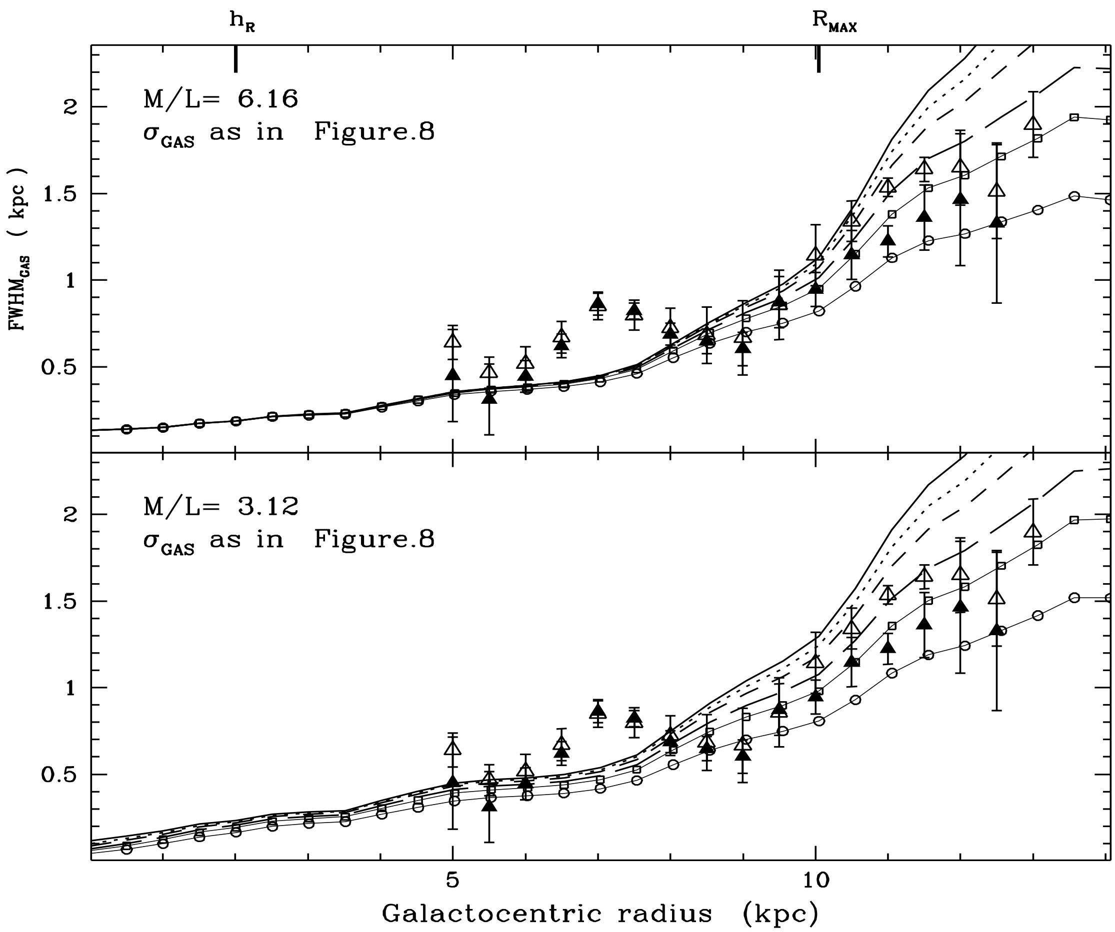

Fig. 29.— The measured widths (open and filled triangles with error bars, for the fixed and varying inclination case, respectively) together with the model widths corresponding to different halo flattenings q_ρ are plotted: q_ρ=1.0, 0.7, 0.5, 0.3, 0.2, and 0.1 from top to bottom. The maximum-disk (top panel) and the minimum-disk (bottom panel) disk-halo decompositions are presented (the structural parameters are given in the caption of Fig. 28). Both the truncation of the stellar disk (at R_{MAX}) and the gaseous self-gravity have been included in the model calculation. The measured gaseous velocity dispersions (Fig. 22) were used in the model calculations. The observed flaring curve is the average of the north-eastern and south-western sides, except in the 6.5 - 9 kpc region, where the north-eastern flaring data is used (see Sec. 3.7.1.). The 7 kpc hump is probably caused by spiral arm streaming motions (Appendix 3.12.). Deemed unreliable in the inner 5 kpc (Sec. 3.5.2.), the measurements from this region are not plotted. All plotted points are essentially independent measurements. Beyond the optical disk, the thickness of the gas layer is strongly influenced by the shape of the dark halo: we infer q_ρ= $0.2^{+0.3}_{-0.1}$. The mass-to-light ratio of the stellar disk is not constrained by these flaring measurements.

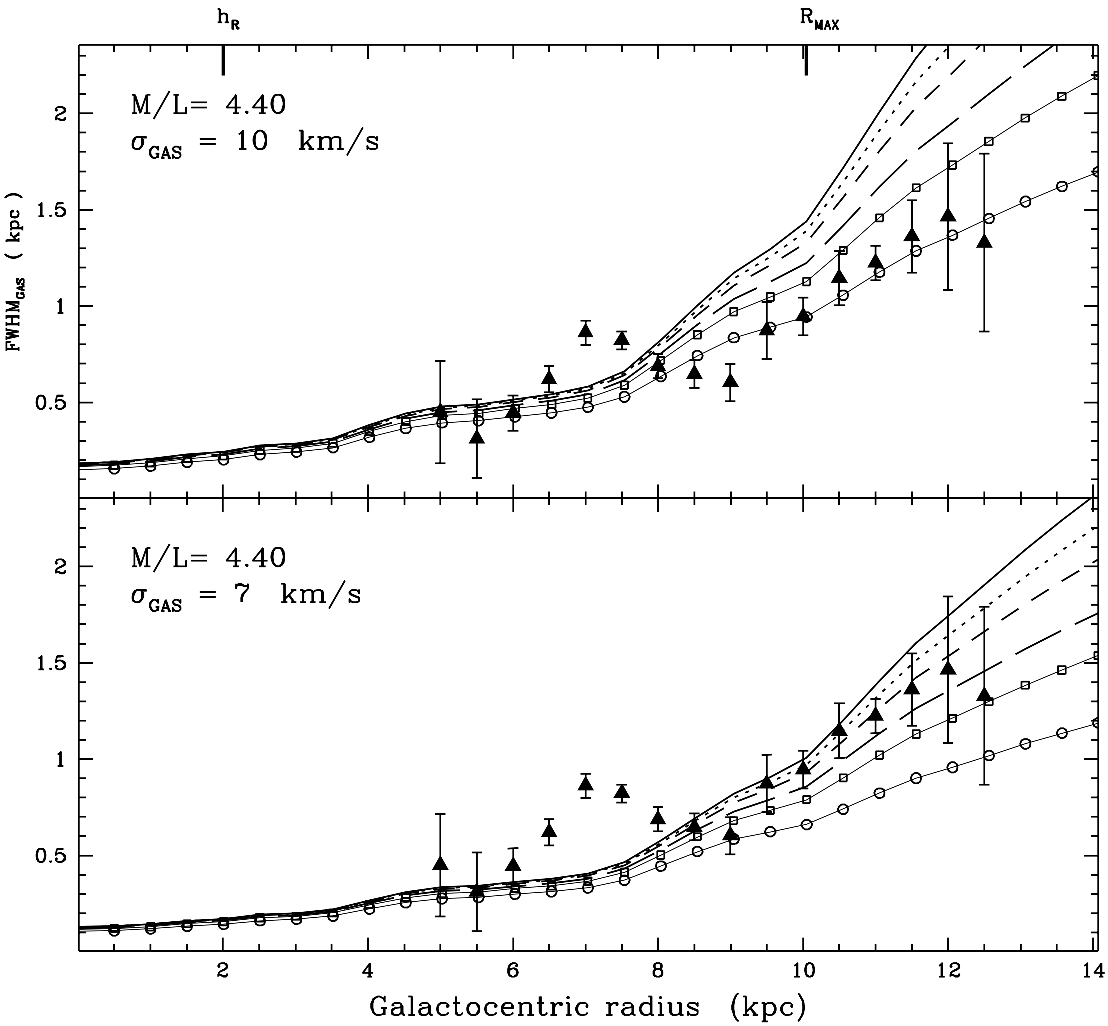

Fig. 30.— The inferred halo flattening depends strongly upon the value of the velocity dispersion. The curves in the top panel (the same labeling of the curves applies as in Fig. 29) are calculated for the "upper limit" of the velocity dispersion as found in the literature. Similarly, the lower panel is calculated for the "lower limit" (see also Sec. 3.7.1.).

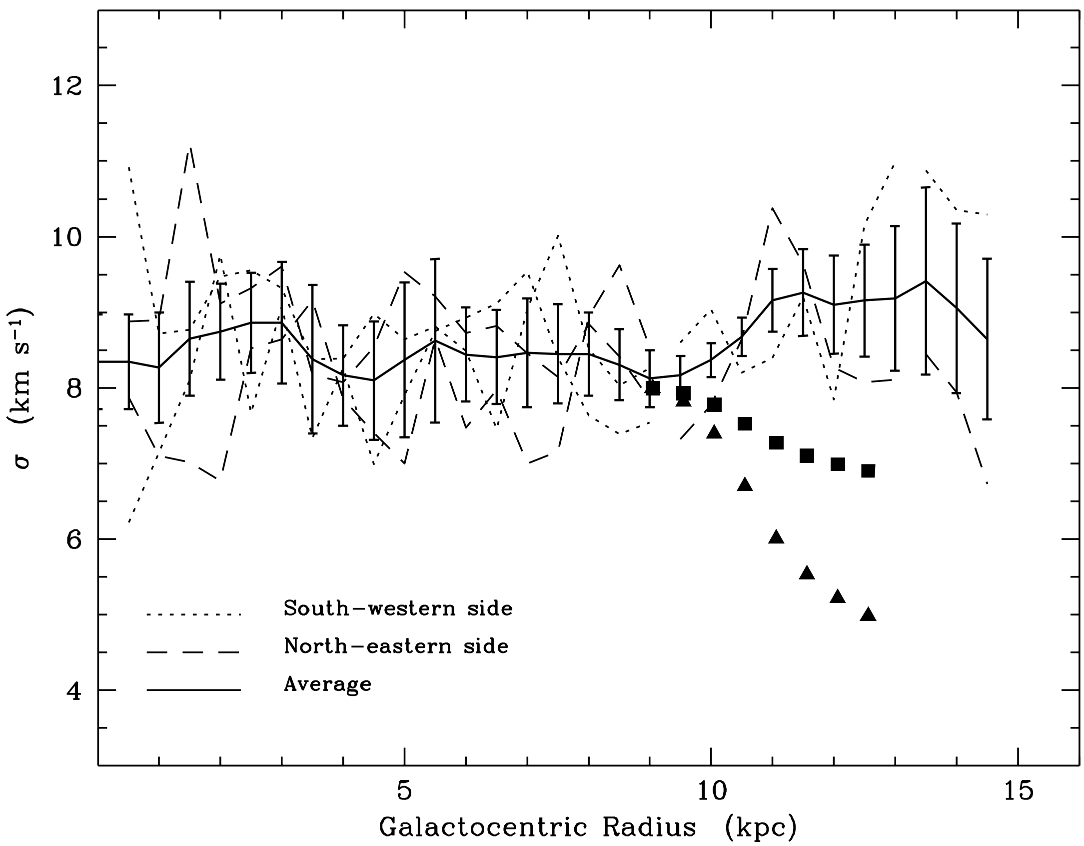

Fig. 31.— The radial variation of the average of the velocity dispersion (full line with the error bars) is presented. The dotted lines are determined from the south-western side, the dashed lines from the north-eastern side (10.″1 and 38″ , for $R \leq 9$ kpc; 38″ and 55″ beyond). For all galactocentric radii, the full line is the average of all curves shown. The filled squares (filled triangles) are the velocity dispersions required to make the model widths for a round halo model consistent with the fixed-inclination (varying-inclination) case flaring measurements (see Sec. 3.7.1.).

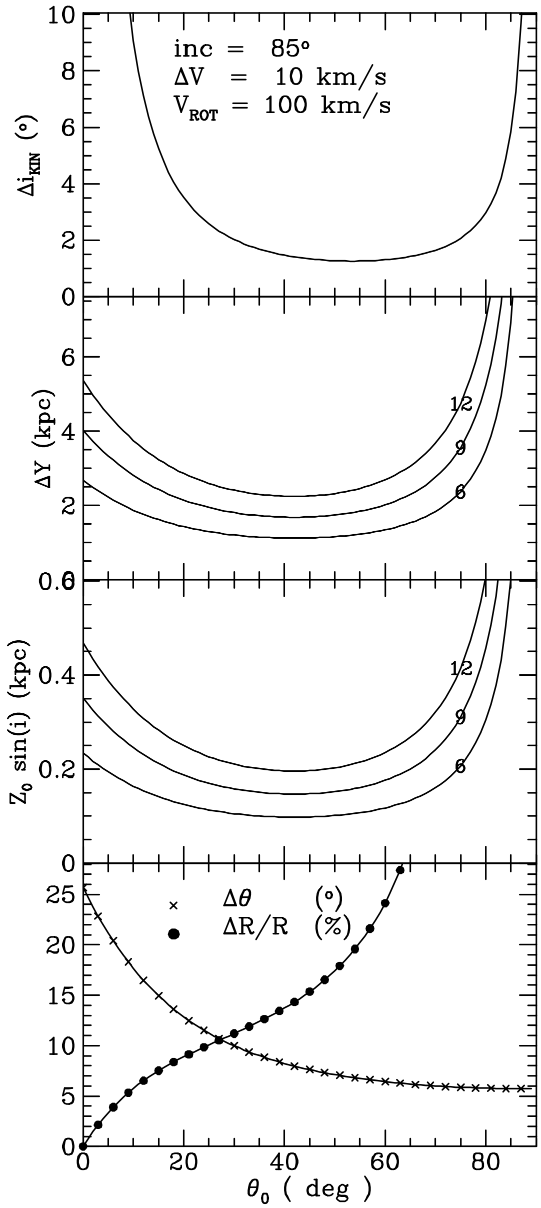

Fig. 32.— This figure illustrates the possible effects of streaming motions on the apparent widths (see Appendix 3.12.). All curves presented scale roughly linearly with the ratio of streaming motion and circular speed. For CSDDs centered on θ_0, I plot the angular width (the lowest panel, crosses) and the normalized range in radius (filled circles) which corresponds to a streaming motion of magnitude ΔV km s^{-1}. The corresponding apparent width on the sky is plotted in the one but lowest panel. In the second panel from the top, I plot the linear distance, in the plane of the galaxy, that the angle $\Delta\theta$ corresponds to. Close to the major and minor axes, long pathlengths reflect a strong sensitivity to small streaming motions. The inclination errors resulting from such streaming motions are plotted in the top panel.

Chapter 4

4. The Channel Surface Density Distributions: CSDDs

4.1. INTRODUCTION

In the previous chapter I described how the thickness of the gas layer can be determined from several channel maps. In order to do so successfully it is imperative to have detailed knowledge of the origin of the emission which is observed at a given velocity channel. In Chapter 3 I indicated that this knowledge can be obtained from the systemic velocity, the measured rotation curve, the measured radial surface density distribution, and the observed gaseous velocity dispersion. With these four parameters known for every point (x, y) in the galaxy, the fraction of the surface density which has a recession velocity equal to the observing velocity is easily calculated. Below I detail this procedure (Sec. 4.2.). Some elementary properties of CSDDs are described in Sec. 4.3.. and the inclination dependence of the method in Sec. 4.4.. I explain the fine details of the method in Sec. 4.5., while the effects of kinematical distortions are discussed in Chapter 3 (Appendix 2.6.).

If the rotation curve is constant, a channel $\Delta V_{\rm chan}$ wide receives flux from gas in a wedge-like region in the plane of the galaxy (Sancisi & Allen 1979, their Fig. 6). For a more realistic galaxy model which includes the observed rotation curve, surface density distribution and gaseous velocity dispersion, these wedges become curved and "wiggly" while the edges are softened. Contour images of several CSDDs are shown in Fig. 24 (Chapter 3). Each CSDD map represents the "face-on view of a channel map", that is to say, the effective local column density distribution a particular velocity channel is sensitive to. When observing at a particular channel we are sensitive to gas in a limited range of azimuths only.

4.2. CALCULATING THE CSDDS

The calculation of the CSDD maps, which requires the observed projected rotation, velocity dispersion, and surface density curves, is straightforward. A CSDD model is represented by a three dimensional array with two spatial and one velocity axes with at least three spatial pixels per beam and the size of the velocity pixel equal to the observing channel width. At each point[35] (x, y) in the plane of the galaxy the projected rotation velocity, $V_{\rm p}$, [onto the line of sight using Eqn. (51) of Chapter 3] and the local H I surface density are determined. Then that local surface density is distributed over velocity space, such that the sum (over all channels j) of the emission seen in each channel,

$$\begin{aligned}\Sigma(x, y, V_{\rm chan}(j)) \quad &= \quad \Sigma_0(x, y) \times \\ &\int_{-\infty}^{\infty} dV_{\rm p}\; S(V_{\rm p}; V_{\rm chan}(j), \Delta V)\; \exp\left(-\frac{1}{2}\left\{\frac{(V_{\rm chan}(j) - V_{\rm p})}{\sigma_{\rm gas}}\right\}^2\right) \qquad (82)\end{aligned}$$

adds up to the observed local H I surface density. Here S is the channel response function as defined in Chapter 3 [Eqn. (62)]. After the calculation of (82) is completed for all pixels, each velocity plane is smoothed to the desired spatial resolution.

[35] The x-axis corresponds to the kinematical major axis of the observed galaxy. See Chapter 3, Sec. 3.4.1., for the definition of the coordinate system.

This calculation is not affected by errors in the determination of the rotation curve or inclination because the projected rotation speed depends on the *product* of $V_{\rm rot}(R)$ and $\sin i(R)$, which can be determined with much greater accuracy than rotation speed or inclination individually (cf. Begeman 1989).

4.3. PROPERTIES OF CSDDS

A line of sight from the observer through the galaxy crosses the major axis at distance x. The emission along these sight lines can be approximated[36] by the sum of two Gaussian [one for the near- and one for the far-side; Eqn. (52), Chapter 3]. The center position, $\pm Y_{\rm C}$, of these two Gaussians depends primarily on the rotation speed. The width, $FWHM_{\rm C}$, of the CSDD depends strongly on the gaseous velocity dispersion and only slightly on the surface density distribution. A general two-component fit on a profile which does not have two distinctive peaks is rather unstable[37], imposing equal amplitude and widths for the components alleviates this problem.

For a "flat" rotation curve, the opening angles of the CSDDs are approximately constant with radius. In Chapter 3 (Appendix 2.6.) it was shown that the the width of the CSDD is approximately proportional to the gaseous velocity dispersion and inversely proportional to the rotation speed [Eqn. (76), Chapter 3]. In a rough approximation, for a typical channel, 40$^{\rm o}$ from the major axis, the width of the CSDD is given by:

$$FWHM_{\rm C}(R;i) \quad \approx \quad (4 \pm 0.5) \left(\frac{\mathrm{MAX}(\sigma_{\rm p,gas}, [\Delta V_{\rm chan}/2])}{V_{\rm rot}\ \sin(i)} \right) \ R \ , \tag{83}$$

where the proportionality constant, determined from Fig. 33, is independent of galaxian properties [cf. Eqn. (76), Chapter 3]. In Sec. 4.4. I show that this slow linear increase of the CSDD's width allows us to determine the thickness of the gas layer down to inclinations of roughly 60$^{\rm o}$.

4.4. THE INCLINATION DEPENDENCE OF THE METHOD

In order to reliably determine the thickness of the gas layer its width projected on the sky needs to be of the same order as, or preferably larger than, the other contributors to the apparent width (beam size and the projected CSDD width).

Beyond the optical disk the radial dependence of the thickness of the gas layer is given by (Chapter 2, Appendix 2.7.):

$$FWHM_{\rm z}(R) \quad \approx \quad 2.35 \left(\frac{\sigma_{\rm z,gas}}{V_{\rm rot,max}} \right) \sqrt{\frac{2.4\ q}{1.4 + q}} \ R \ , \tag{84}$$

where $\sigma_{\rm z,gas}$ is the vertical gaseous velocity dispersion, $V_{\rm rot,max}$ the maximum rotation speed, and q the axial ratio of the DM halo: the thickness of the gas layer increases linearly with radius. The planar width of the CSDD also increases linearly with radius [Eqn. (83)] Furthermore, the width of

---

[36]Typically deviations of the order of 5-10% occur. At some locations the profiles can be rather non Gaussian, however the potential errors resulting from streaming motions are more important (see Chapter 3, Appendix 2.6.).

[37] One type of two-component solution consists of two components of the same width, centered at the origin, each contributing half of the total amplitude. A second type of solution consists of the superposition of a broad and a narrow component centered at the origin. A third type of solution consists of the components separated by some amount. If the data is noisy and/or has some broader non-Gaussian wings, the solutions of a non-restrictive two-component Gaussian fit tend to switch between the three type of possible solutions in a noise-dominated manner.

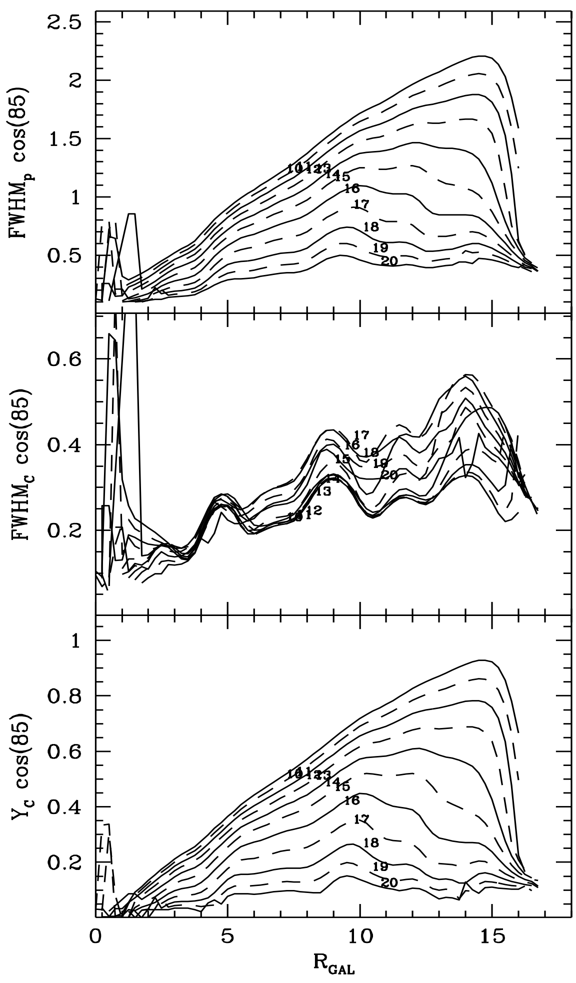

Fig. 33.— This figure shows, for some channels, the fitted center position (lower panel), the width (middle panel) and the effective width (upper panel) of the CSDD, all projected onto the plane of the sky. The channels numbers are indicated at various positions along the curves. For most channels the effective width is mostly due to the projected separation of the near and far side of the CSDDs ($Y'_{\rm C} = Y_{\rm C}\ \cos i$). The low velocity channels have effective widths ($FWHM_{\rm EFF} = FWHM_{\rm p}\ \cos i$) comparable to the intrinsic thickness of the gas layer ($FWHM_{\rm z}$), and will hence contribute most to the error on the determined thickness.

the CSDD varies approximately linearly with gaseous velocity dispersion. The ratio of vertical to planar projected widths [from Eqns. (84) and (83)]

$$\left(\frac{FWHM_{\rm z}\ \sin i}{FWHM_{\rm C}\ \cos i}\right) \approx (0.59 \pm 0.07)\ \sin i\ \tan i \left(\frac{\sigma_{\rm z,gas}\sqrt{2.4\ q/(1.4+q)}}{{\rm MAX}(\sigma_{\rm p,gas}, \left[\frac{1}{2}\Delta V_{\rm chan}\right])}\right)\ , \tag{85}$$

depends on the inclination of the system, the ratio of vertical to planar gaseous velocity dispersion, and the flattening of the DM halo. This ratio is independent of rotation speed and galactocentric radius. If the observing channel widths are smaller than twice the planar velocity dispersion ($\sigma_{\rm p,gas}$), and if the velocity dispersion is isotropic, then only the flattening and inclination dependencies remain. Demanding that the ratio of vertical to planar projected widths is larger than unity excludes systems inclined less than about 60$^{\rm o}$ (for the case of a round DM halo). This inclination cutoff is confirmed by numerical experiments (Chapter 3, Fig. 25).

4.5. THE PRACTICAL IMPLEMENTATION OF THE METHOD

To facilitate the extraction of data at a given galactocentric radius I regrid both the observations and the CSDDs in such a way that the major axis coordinate is transformed from projected radius to galactocentric radius. By calculating the CSDD maps at the same resolution as the data, systematic effects due to gradients in the beam are minimized. For each individual channel a galactocentric radius R ($\equiv \sqrt{x^2 + Y_{\rm C}^2}$) is assigned to each projected distance x. For each pixel along the major axis a quadratic function, describing